

# FERMI-LAT OBSERVATIONS OF EXTENDED GAMMA-RAY EMISSION IN THE DIRECTION OF SNR G150.3+4.5

JAMIE M. COHEN, DANIEL CASTRO, ELIZABETH HAYS, JOHN W. HEWITT

## ABSTRACT

We report here a dedicated analysis of the  $\gamma$ -ray emission around supernova remnant (SNR) G150.3+4.5, observed with the Large Area Telescope (LAT) on board the *Fermi Gamma-Ray Space Telescope*. The Second Catalog of Hard *Fermi*-LAT Sources reported detection of a hard spectrum, spatially extended source from 50 GeV - 2 TeV, partially overlapping G150.3+4.5. Lowering the energy threshold to 1 GeV, we significantly detect a large ( $\sigma = 1.40^\circ \pm 0.03^\circ$ ) extended  $\gamma$ -ray source consistent with the entirety of the radio shell and displaying a power law spectral index of  $1.82 \pm 0.04$ . An obtained HI spectrum toward the SNR suggests that the remnant could be one of the closest to us. Estimates of its age, within the context of other LAT observed SNRs, indicate that G150.3+4.5 is in the Sedov-Taylor phase, and is compatible with a dynamically-young remnant. Despite the spectral similarities with other unevolved SNRs, ROSAT all-sky survey observations show no prominent X-ray emission in the region. We model the broadband non-thermal radiation from G150.3+4.5 using a published radio spectrum of the SNR and the GeV results presented here. We find that the emission is best described by [JAM: or, can be described equally well by blah. End with the naima results plus possibly young close SNR]

**Keywords:** Supernova Remnants,  $\gamma$ -rays, Cosmic rays, Radio

## 1. INTRODUCTION

SNRs have long been thought to be the most-likely accelerators of cosmic rays up to the knee of the CR energy spectrum, with diffusive shock acceleration being the primary mechanism accelerating the charged particles to  $\gamma$ -ray emitting energies (see Reynolds (2008) for a review of SNRs from X-rays to  $\gamma$ -rays). *Fermi*-LAT was instrumental in demonstrating that CR protons can indeed be accelerated by SNR shock fronts (through detection of the characteristic "pion bump" feature), and are capable of generating the observed  $\gamma$ -ray emission in SNRs (Ackermann et al. 2013; Jogler & Funk 2016). In addition, observations of SNRs with the LAT have proven to be vital in uncovering a large swath of the  $\gamma$ -ray SNR population; both evolved SNRs interacting with dense surrounding material, as well as dynamically young remnants useful for probing acceleration directly at the shock (Acero et al. 2016).

The recently updated LAT Pass 8 event reconstruction provides a significantly improved angular resolution, acceptance, and background event rejection (Atwood et al. 2013a,b) all of which lead to an increase in the effective energy range and sensitivity of the LAT. Leveraging the increased sensitivity afforded by Pass 8 data, Ackermann et al. (2016) performed an all-sky analysis from 50 GeV to 2 TeV (referred to as the second catalog of hard *Fermi*-LAT sources, or 2FHL), directly connecting GeV LAT observations with those of ground-based Cherenkov telescopes at higher energies. While it is troublesome for Cherenkov telescopes operating under pointed observations to detect broadly extended sources on the sky (i.e. sources larger than the telescopes field of view (FOV)), the LAT, with its all-sky survey mode and wide FOV, is well suited for this task. The 2FHL catalog detected significant spatial extension from 31 sources above 50 GeV, 5 of which had not previously been detected as extended.

Of particular interest, one of the 5 blindly de-

tected sources, 2FHL J0431.2+5553e, was a large extended source (modeled as a uniform disk with radius,  $\sigma = 1.27^\circ \pm 0.04^\circ$ ), exhibiting a hard power-law spectral index ( $\Gamma = 1.66 \pm 0.20$ ). This 2FHL source was found to be coincident with a recently detected radio SNR, G150.3+4.5. Faint emission from the eastern portion of the shell of G150.3+4.5 was first reported in Gerbrandt et al. (2014) (called G150.8+3.8), and considered a strong SNR candidate due to the semi-circular shape of the emission, clearly non-thermal spectrum, and the presence of red optical filamentary structures. Gao & Han (2014) performed follow-up observations of the region using Urumqi 6 cm survey data (as well as Effelsberg 11cm and 21cm data and CGPS 1420 MHz and 408 MHz observations), taking advantage of the survey's extended Galactic latitude range, up to  $b=20^\circ$ . They reported clear detection of a  $2.5^\circ$  wide by  $3^\circ$  high, synchrotron emitting, shell-like object (G150.3+4.5), bolstering an SNR origin for the radio emission.

2FHL J0431.2+5553e only partially overlaps the northern region of G150.3+4.5, so the nature of the extended  $\gamma$ -ray source is uncertain. In this paper, we present an in depth study of the  $\gamma$ -ray emission in the direction of SNR G150.3+4.5, extending the energy from 50 GeV (as in 2FHL), down to 1 GeV. We report here detection of a significantly extended source whose extent matches well with that of G150.3+4.5. We describe the LAT observations and explore the spectral and spatial properties of the extended  $\gamma$ -ray source in § 2. In § 3 we employ archival HI and X-ray observations to assess the properties of the environment G150.3+4.5 resides in. Finally, in § 4 we discuss potential  $\gamma$ -ray emission scenarios and model the broadband emission from the source to constrain the origin of the GeV emission and understand the connection between the radio-detected, SNR G150.3+4.5, and the  $\gamma$ -ray source.

2. *Fermi*-LAT OBSERVATIONS AND ANALYSIS2.1. *Data Set and Reduction*

*Fermi*-LAT is a pair conversion telescope sensitive to high energy  $\gamma$ -rays from 20 MeV to greater than 1 TeV (Ackermann et al. 2016), operating primarily in a sky-survey mode which covers the entire sky every 3 hours. The LAT has a wide field of view ( $\sim 2.4$  sr), a large effective area of  $\sim 8200$  cm<sup>2</sup> at 1 GeV for on-axis events, and a 68% containment radius angular resolution of  $\sim 0.8^\circ$  at 1 GeV. For further details on the instrument and its performance see Atwood et al. (2009) and Ackermann et al. (2012).

In this study, we analyzed 7 years of Pass 8 data, from August 2nd 2008 to August 2nd 2015. Source class events were analyzed within a  $14^\circ \times 14^\circ$  region centered on SNR G150.3+4.5 using the P8R2\_SOURCE\_V6 instrument response functions, with a pixel size of  $0.1^\circ$ . To reduce contamination from earth-limb  $\gamma$ -rays, only events with zenith angle less than  $100^\circ$  were included.

For spectral and spatial analysis we utilized both the standard *Fermi* Science Tools (version 10-01-01)<sup>1</sup>, and the binned maximum likelihood package *pointlike* (Kerr 2010). *pointlike* provides methods for simultaneously fitting the spectrum, position, and spatial extension of a source, and was extensively validated in Lande et al. (2012). Both packages fit a source model, the Galactic diffuse emission, and an isotropic component (which accounts for the background of misclassified charged particles and the extragalactic diffuse  $\gamma$ -ray background) to the observations. In this analysis, we used the standard Galactic diffuse ring-hybrid model scaled for Pass 8 analysis, *gll\_iem\_v06.fits* (modulated by a power law function with free index and normalization), and for the isotropic emission, we used *iso\_P8R2\_SOURCE\_V6\_v06.txt*, extrapolated to 2 TeV as in Ackermann et al. (2016).

In our source model for the region, we included sources from the third *Fermi*-LAT catalog (Acero et al. 2015, 3FGL) within  $15^\circ$  of the center of our region of interest (RoI). We replaced the position and spectrum of any 3FGL pulsars in the region with their corresponding counterpart from the LAT 2nd pulsar catalog (Abdo et al. 2013). Residual emission unaccounted for by 3FGL sources is present in the RoI due to the increased time range and different energy selection with respect to that in 3FGL. We added to the RoI several point sources ( $\geq 4\sigma$  detection significance) to account for this unmodeled emission and minimize the global residuals. The closest of these sources added was over  $1^\circ$  away from the edge of the best fit GeV disk (discussed in §2.2). Considering the size of the point spread function (PSF) at 1 GeV, the affect of these sources on the disk fit was assumed to be negligible and we do not discuss them further. The normalization and spectral index of sources within  $5^\circ$  of the center of the RoI were free to vary, whereas all other source parameters were fixed. A preliminary maximum likelihood fit of the RoI was performed, and sources with a test statistic (TS)  $< 9$  (TS is defined as,  $TS \equiv 2 \log(\mathcal{L}_1/\mathcal{L}_0)$  where  $\mathcal{L}_1$  is the likelihood of source plus background and  $\mathcal{L}_0$  that of just the background) were removed from the model.

<sup>1</sup> <http://fermi.gsfc.nasa.gov/ssc/>

2.2. *Morphological Analysis*

Studying the spatial extension of sources with the LAT is non-trivial due to the energy-dependent PSF and strong diffuse emission present in the Galactic plane. Soft spectrum point sources and uncertainties in the diffuse model can act as sources of systematic error when not accurately modeling extended emission as such, particularly at low energies where the PSF is broad. To strike a balance between the best angular resolution and minimal source and diffuse contamination, we restricted our morphological analysis to energies between 1 GeV and 1 TeV. We divided this energy range into 12 logarithmically spaced bins for both *pointlike* and *gtlike* binned likelihood analyses.

Three unidentified 3FGL sources are located within the extent of G150.3+4.5. 3FGL J0425.8+5600, located approximately  $0.6^\circ$  from the center of the SNR, is the closest of the three sources, and is described with a power law spectrum of index  $\Gamma = 2.35 \pm 0.17$  in the 3FGL catalog. The closest radio source to 3FGL J0425.8+5600 is NVSS J042719+560823, at  $0.25^\circ$  away (Condon et al. 1998). 3FGL J0423.5+5442, exhibits a power law spectral index,  $\Gamma = 2.63 \pm 0.15$ , with no clear multiwavelength counterpart. Finally, 3FGL J0426.7+5437 has a pulsar-like spectrum, yet in a timing survey performed with the 100-m Effelsberg radio telescope, Barr et al. (2013) were unable to detect pulsations from the source down, to a limiting flux density of  $\sim 0.1$  mJy. This source is located about  $0.84^\circ$  from the center of the SNR. We discuss 3FGL J0426.7+5437 and potential association with G150.3+4.5 further in § 4.2. Figure 1 is a counts map of the region, showing the location of the 3FGL sources.

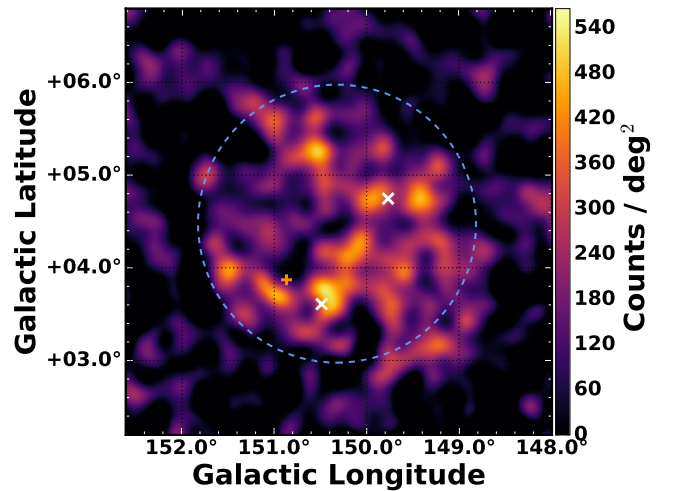


**Figure 1.** Smoothed background subtracted residual counts map above 1 GeV, centered on SNR G150.3+4.5. The  $0.1^\circ \times 0.1^\circ$  pixels were smoothed with a Gaussian kernel of  $0.1^\circ$ . 3FGL J0426.7+5437 (shown as the orange cross) and the diffuse backgrounds are included in the region model, however 3FGL J0425.8+5600 and 3FGL J0423.5+5442 are not (but their locations are shown as white crosses). The blue, dashed circle corresponds to the extent of the radio SNR.

In our analysis, we removed 3FGL J0425.8+5600 and 3FGL J0423.5+544 from the RoI, but kept 3FGL J0426.7+5437 in the model since preliminary analyses showed clear positive residual emission at the position of the source if it was removed from the RoI. Figure 2 shows

a residual TS map for the region around G150.3+4.5. This point source detection-significance map was created by placing a point source (modeled with a power law of photon index  $\Gamma = 2$ ) at each pixel and performing a likelihood fit of the region. It gives the significance of detecting a point source at each location above the background.

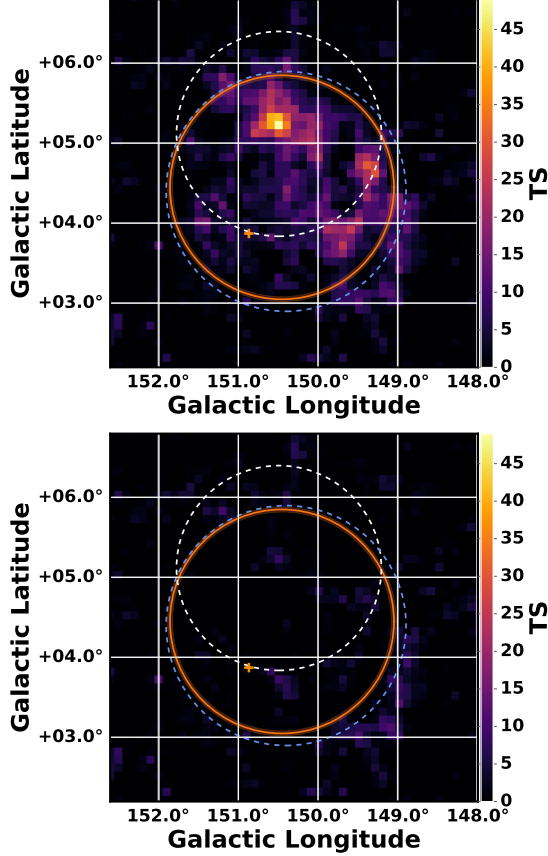


**Figure 2.** Background subtracted residual TS map above 1 GeV with  $0.1^\circ \times 0.1^\circ$  pixels, centered on SNR G150.3+4.5. The orange circle and translucent shading show the fit disk radius and  $1\sigma$  errors, respectively, for the extended source. The orange cross shows the position of 3FGL J0426.7+5437 (included in the background model). Blue dashed circle is the extent of the radio SNR, and white dashed circle depicts 2FHL J0431.2+5553e. Bottom map includes G150.3+4.5 in the background model, top does not.

We modeled the excess emission in the direction of G150.3+4.5 with a uniform intensity, radially-symmetric disk, simultaneously fitting the spatial and spectral components of the model via *pointlike*. The extension of the disk was initialized with a seed radius of  $\sigma = 0.1^\circ$  and position centered on the radio position of G150.3+4.5. We define the significance of extension as in Lande et al. (2012);  $TS_{\text{ext}} = 2 \log(\mathcal{L}_{\text{ext}}/\mathcal{L}_{\text{ps}})$ , with  $\mathcal{L}_{\text{ext}}$  being the likelihood of the model with the extended source and  $\mathcal{L}_{\text{ps}}$  that of a point source located at the peak of emission interior to the extended source. For the disk model we found that  $TS_{\text{ext}} = 298$ , for the best fit radius,  $\sigma = 1.40^\circ \pm 0.03^\circ$ , and position, R.A. =  $55.46^\circ \pm 0.03^\circ$ , DEC. =  $66.91^\circ \pm 0.03^\circ$ , all in excellent agreement with the radio SNR size and centroid determined in Gao & Han (2014). Figure 3 shows the radially integrated counts for the region as a function of angular radius

squared. It is clear from this figure that there is a significant excess of counts above the Galactic diffuse radiation in this region that is adequately modeled by a symmetric disk. We tried adding back in to our model the two removed 3FGL sources but both were insignificant when fit on top of the best fit disk. The bottom map in Figure 2 is a residual TS map of the same region as the top map, but with the disk source included in the background model, demonstrating that the disk can account well for the emission in the region and justifying the exclusion of the two aforementioned 3FGL sources.

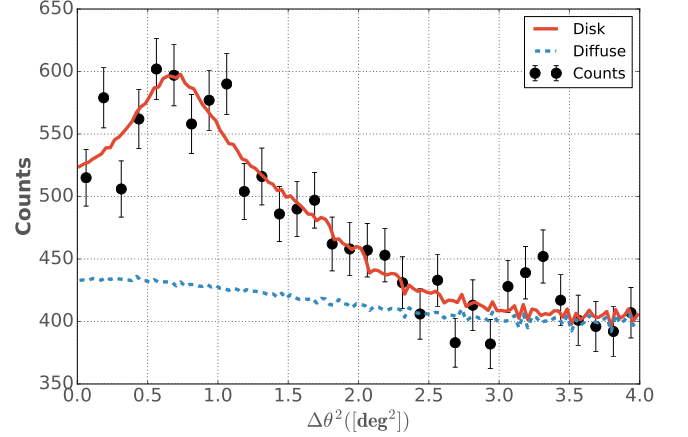


**Figure 3.** Radially integrated counts map centered on the GeV emission coincident with G150.3+4.5. Red line shows the expected counts for a uniform intensity disk with radius,  $\sigma = 1.40^\circ$ , blue line is that of the Galactic diffuse background.

The morphology of the radio emission is suggestive of an elliptical or ring morphology, so both of these spatial models were tested as well. For the ring model, the fit reduced to a disk with parameters matching those stated above. Using the elliptical model showed a weak improvement over the radially symmetric model at the  $2.6\sigma$  level ( $\Delta TS = 9$  with two additional degrees of freedom), which we did not consider significant enough to say the GeV emission had an elliptical morphology (see Table 1). For the remainder of this study, we only considered the disk spatial model.

2FHL J0431.2+5553e is the extended source detected in the 2FHL catalog found to be overlapping the northern region of G150.3+4.5 (Ackermann et al. 2016). The source has a power law spectral index  $\Gamma = 1.66 \pm 0.2$ , and disk radius  $\sigma = 1.27^\circ \pm 0.04^\circ$  (see Figure 2). When comparing the best fit extension of the 2FHL source with the result from this paper, factoring in the uncertainty in both extension and position, we see that the  $\geq 50$  GeV and  $\geq 1$  GeV results are not incompatible. It is possible that the paucity of events above 50 GeV is the cause of the smaller fit radius, as opposed to the difference arising from the effects of an energy dependent morphology. To explore the connection between the 2FHL source and the one detected here above 1 GeV, we tested several other spatial hypotheses. [JAM: maybe this isn't true if VERITAS is seeing a similar source to the 2FHL source? Or do they not have sensitivity there too?]

First, we replaced the  $\sigma = 1.40^\circ$  disk with another disk matching the spectral and spatial parameters of 2FHL J0431.2+5553e and calculated the likelihood with this



new source's position and extension fixed. For this hypothesis, we find  $TS_{\text{ext}} = 165$ , and  $TS = 226$ , demonstrating that the fixed disk matching the 2FHL source is clearly disfavored over the previously determined best-fit disk at this energy. Our next test consisted of placing a second extended source on top of the best fit disk detected above 1 GeV. We added a source, initially matching the spatial and spectral parameters of 2FHL J0431.2+5553e, to our source model of the region (in addition to the  $\sigma = 1.40^\circ$  disk), and fit its spectrum and extension. Fitting a second extended source in this region serves two purposes: 1. it acts as a check on whether there was residual emission unaccounted for by the previously best-fit disk, and 2. it allows us to determine if the best fit disk can be split into two spectrally distinct components. This fit resulted in the source wandering north (but still partially overlapping G150.3+4.5) and having an insignificant extension,  $TS_{\text{ext}} = 4$ . Details on the spatial parameters are given in Table 1.

### 2.3. Spectral Analysis

After determining the best fit morphology with `pointlike` for the GeV emission coincident with G150.3+4.5, we used those results as a starting point for our `gtlike` maximum-likelihood fit of the region to estimate the best spectral parameters for our model. The LAT data is well described by a power law from 1 GeV to 1 TeV with a photon index,  $\Gamma = 1.82 \pm 0.04$ , and energy flux above 1 GeV of  $(7.3 \pm 0.72) \times 10^{-11} \text{ erg cm}^{-2} \text{ s}^{-1}$  and  $TS = 389$ . We tested the  $\gamma$ -ray spectrum of the extended disk for spectral curvature using a log-normal model (Log Parabola), and find no significant deviation from a power law ( $\Delta TS \sim 1$ ). Figure 4 shows the best-fit power law spectral energy distribution (SED) for the GeV source whose morphology was described in Section 2.2. Spectral data points were obtained by dividing the energy range into 12 logarithmically spaced bins and modeling the source with a power law of fixed spectral index,  $\Gamma = 2$ . We overplotted the SED of 3FGL J0426.7+5437 to demonstrate how the spectra of the two sources are comparable in the lowest energy bin and would grow more confused at energies below 1 GeV.

## 3. MULTIWAVELENGTH OBSERVATIONS AND ANALYSIS

### 3.1. HI Observations and Distance Estimate

Using data from the Leiden/Argentine/Bonn survey of Galactic HI, we obtained the HI spectrum in the direction of G150.3+4.5. The spectrum shown in Figure 5 displays clear velocity peaks at  $-44.7$ ,  $-35.9$ ,  $-6.9$  and  $+2.9 \text{ km s}^{-1}$ . The widths of all peaks are  $5 \text{ km s}^{-1}$  or less, thus there is no evidence of shock-broadening from the SNR shock, where broadening is an indicator of the shock of an SNR overtaking nearby molecular clouds Wootten (1977, 1981).

Knowing the distance to G150.3+4.5 is integral in determining the physical size of the SNR and in turn understanding the origin of the  $\gamma$ -ray emission. We calculate the kinematic distance to G150.3+4.5 as in Reid et al. (2014), assuming a flat Galactic rotation curve with Galactocentric distance,  $R_0 = 8.34 \text{ kpc}$ , and circular rotation speed at the sun,  $\Theta = 240 \text{ km s}^{-1}$ . For the three negative velocities noted above (the positive velocity is not permitted at this Galactic longitude), we determine distances of 5.6, 3.9, and 0.38 kpc respectively.

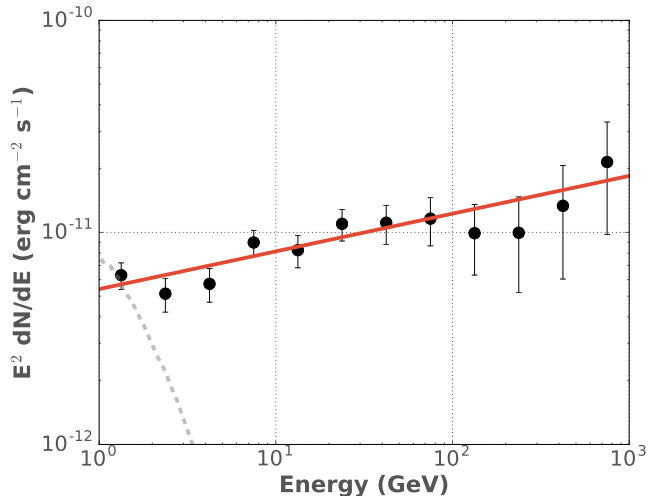


**Figure 4.** SED for the extended source coincident with SNR G150.3+4.5 from 1 GeV to 1 TeV. Red line corresponds to the best-fit power law model. Points are shown with statistical error bars. Grey dashed line is the SED of 3FGL J0426.7+5437, modeled with an exponential cut-off power law.

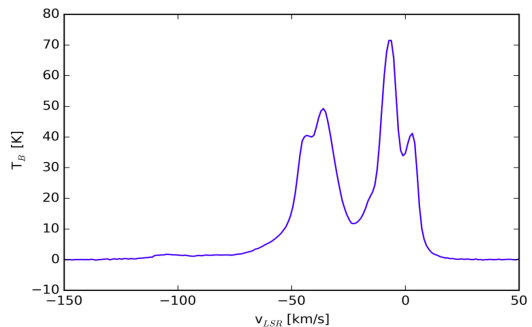


**Figure 5.** G150.3+4.5 HI spectrum.

For an angular radius of,  $\sigma = 1.40^\circ$  (as determined in §2.2), these distances correspond to physical radii of 135.8, 96.3, and 9.4 pc. The two further distances, and hence larger radii, are indicative of an SNR in the radiative phase of evolution. However, at this late stage of evolution, the shock front of an SNR will have expanded, losing much of its initial energy, and is not expected to be capable of accelerating CRs to  $\gamma$ -ray energies. Thus, the only feasible distance, derived from the HI velocities, is the nearest distance,  $d_{\text{near}} \approx 0.38 \text{ kpc}$ .

There are two HII regions known to lie at the edge of the SNR shell, so it is reasonable to think there may be a physical association between the clouds and the SNR. Lying at a distance (in projection) of 4 kpc (Gao & Han 2014), the physical radius of the SNR, if it was at the same distance, would be  $\approx 98 \text{ pc}$ . Aside from the proximity (in projection), there is no evidence to suggest that the clouds are physically associated with the SNR. In fact, the lack of ROSAT X-ray emission in the vicinity of the G150.3+4.5 (see §3.2), suggests that the SNR is not associated with the cloud at all. Another potential scenario is that the SNR lies in the Perseus spiral arm of the Galaxy at a distance of 2 kpc (Xu et al. 2006). At that distance, the physical extent of the SNR would be  $\approx 49 \text{ pc}$ . Again, an SNR of this size is not expected to emit  $\gamma$ -rays[JAM: be careful here! Is this the radius or diam? Cygnus loop has an estimated size of 70pc].

**Table 1**  
Extended Source Analysis Results

Spatial Model	TS <sub>ext</sub>	TS	$\sigma$ [°]	R.A. [°]	DEC [°]	Index
Disk	298	410	$1.40^\circ \pm 0.03^\circ$	$66.91^\circ \pm 0.03^\circ$	$55.46^\circ \pm 0.03^\circ$	$1.82 \pm 0.04$
Elliptical Disk	341	419	$1.77^\circ/1.23^\circ \pm 0.02^\circ$	$66.61^\circ \pm 0.04^\circ$	$55.43^\circ \pm 0.03^\circ$	$1.82 \pm 0.04$
2FHL (fixed)	165	226	1.29	67.8	55.80	$1.73 \pm 0.05$
Disk & 2FHL	4	17	$0.80^\circ \pm 0.04^\circ$	$69.33^\circ \pm 0.06^\circ$	$56.00^\circ \pm 0.06^\circ$	$1.34 \pm 0.17$

**Note.** — For the elliptical disk model,  $\sigma$  gives the semi-major and semi-minor axes, whereas for the other models,  $\sigma$  is the disk radius. 2FHL (fixed) corresponds to the model where 2FHL J0431.2+5553e was included with spatial parameters fixed. In the Disk & 2FHL model, we included both the best-fit disk determined in §2.2, fixed in position and size, and added a source resembling 2FHL J0431.2+5553e with free spectral and spatial parameters. This model reports the fit values of 2FHL J0431.2+5553e

A final note on possible distances for G150.3+4.5; [Badenes et al. \(2010\)](#) observed a cutoff in the size distribution of  $\approx 60$  pc for SNRs in the small and large Magellanic clouds as well as M33. This suggested that there may be a universal cutoff in size for SNRs. If the physical diameter of G150.3+4.5 was 60 pc, this would place the SNR at a distance  $d_{\text{max}} = 1.2$  kpc. While there is no physical reason to suggest that the SNR is at this distance, it is a reasonable distance/size combination for the SNR to still be emitting  $\gamma$ -rays. We consider this a maximum distance for the SNR.

### 3.2. X-ray Observations

We used archival observations from the ROSAT all-sky survey ([Voges et al. 1999](#)) to determine if there was significant X-ray emission (0.4 keV – 2.4 keV) in the direction of G150.3+4.5. The ROSAT data was extracted within a  $1.3^\circ$  radius centered on the SNR with a total exposure of 5.37 hr. To determine an upper limit on the X-ray emitting density, we modeled the emission (via XSPEC) as an absorbed thermal NEI plasma with  $kT = 0.5$  keV. The derived maximum emitting density was found to be  $n_H < 0.02(D/1 \text{ kpc})^{-1/2} \text{ cm}^{-3}$ , with a maximum photon flux of  $0.04 \text{ ph cm}^{-2} \text{ s}^{-1}$ , and corresponding maximum energy flux of  $4 \times 10^{-11} \text{ erg cm}^{-2} \text{ s}^{-1}$  between 0.5 and 2 keV. We also simulated the emission from the region with an absorbed non-thermal power law model to assess any potential synchrotron flux from the SNR. Using a power law with spectral index  $\Gamma = 2$ , we find a maximum flux of  $0.03 \text{ ph cm}^{-2} \text{ s}^{-1}$ , and corresponding maximum energy flux of  $5 \times 10^{-11} \text{ erg cm}^{-2} \text{ s}^{-1}$ .

Assuming the near distance calculated in §3.1, the maximum emitting density is  $n_H < 0.02(D/1 \text{ kpc})^{-1/2} \text{ cm}^{-3} = 0.03 \text{ cm}^{-3}$ . Under standard shock conditions, the shock compression ratio is 4, and the corresponding, maximum ambient density (that of the unshocked medium), rarefied by a factor of 4, is  $n_0 < 0.008 \text{ cm}^{-3}$ . If instead we use the maximum distance,  $d_{\text{max}} = 1.2$  kpc discussed in §3.1, we find that  $n_H < 0.018$ , and  $n_0 < 0.05 \text{ cm}^{-3}$ .

## 4. DISCUSSION AND RESULTS

### 4.1. G150: Supernova Remnant or Pulsar Wind Nebula?

The follow-up observations of the  $\gamma$ -ray emission in the direction of G150.3+4.5, presented here, of the source detected above 50 GeV in 2FHL have led to the detection of an extended  $\gamma$ -ray source whose centroid and radius match extremely well with those of the radio detected

SNR. The broad size of the extended source and correlation with the radio shell leaves few plausible scenarios for the nature of the GeV emission. Namely, the GeV emission can arise from the wind nebula of the putative pulsar of G150.3+4.5 or the GeV emission corresponds to  $\gamma$ -rays produced in the SNR. We argue here that the SNR is favored over a pulsar wind nebulae (PWN) as the generator of the observed  $\gamma$ -rays.

The first problem with the PWN hypothesis is that there is no pulsar candidate detected near the centroid of the SNR to power a PWN. While 3FGL J0425.8+5600 is the closest  $\gamma$ -ray source to the center of the remnant, it does not have a pulsar-esque spectrum, it lies about  $0.25^\circ$  away, and we showed in §2.2 that with the best-fit disk hypothesis, neither 3FGL J0425.8+5600 nor 3FGL J0423.5+5442 are significant in the likelihood model of the region. 3FGL J0426.7+5437, with a spectrum reminiscent of a pulsar, may actually be one, but as discussed previously, [Barr et al. \(2013\)](#) detect no pulsations from the source. Furthermore, the source is  $0.84^\circ$  away from the centroid of G150.3+4.5. Typical pulsar ballistic velocities range from  $V_{\text{PSR}} \sim 400 - 500 \text{ km s}^{-1}$ , with extreme velocities exceeding  $1000 \text{ km s}^{-1}$  ([Gaensler & Slane 2006](#)). If 3FGL J0426.7+5437 was the compact remnant of the progenitor star that birthed G150.3+4.5, it would have to be traveling with a velocity,  $V_{\text{PSR}} = 1125 \text{ km s}^{-1}$  (assuming an age of 5 kyr, which we derive in the following section, §4.2), and would make it one of the fastest known pulsars ([Chatterjee et al. 2005](#)) [JAM: this number would be even higher for the 500 year age, include that and an estimate of speed if the SNR is at 1.2 kpc]. While possible, this scenario is unlikely without further evidence to support such a high velocity. [JAM: Fastest pulsar (till 2011 at least) 1100 km/s, more recent ref?]

Another argument disfavoring the PWN scenario is that, despite the hard  $\gamma$ -ray spectral index extending to TeV energies, ROSAT X-ray observations detect no significant emission suggestive of a PWN in the direction of G150.3+4.5 (see §3.2). Typical PWN spectral indices range from about  $-0.3 \lesssim \alpha \lesssim 0$  ([Gaensler & Slane 2006](#)). The radio spectral index as determined in [Gao & Han \(2014\)](#) ( $\alpha = 0.4 \pm 0.17$  for part of the eastern shell,  $\alpha = 0.69 \pm 0.24$  for a region in western shell) suggests that the radio object is likely not a PWN.

Many of the arguments disfavoring the PWN hypothesis in fact support that of an SNR. First and foremost in favor of an SNR origin for the  $\gamma$ -ray emission is the excellent agreement between the GeV best-fit disk radius and centroid with that of the radio shell. The radio shell-like

appearance, non-thermal radio spectrum, and strands of red optical filamentary structures led both Gao & Han (2014) and Gerbrandt et al. (2014) to regard the radio source an SNR as opposed to a PWN. The radio spectral index, while not quite in line with typical PWN spectra, is actually common of SNRs.

While the above factors lend credence to an SNR origin for the GeV  $\gamma$ -rays, the PWN scenario can not be ruled out due to the lack of an associated pulsar. Regardless, for the remainder of this study, we assumed the observed  $\gamma$ -rays were produced in the shock front of SNR G150.3+4.5

#### 4.2. G150.3+4.5 in a Supernova Remnant Context

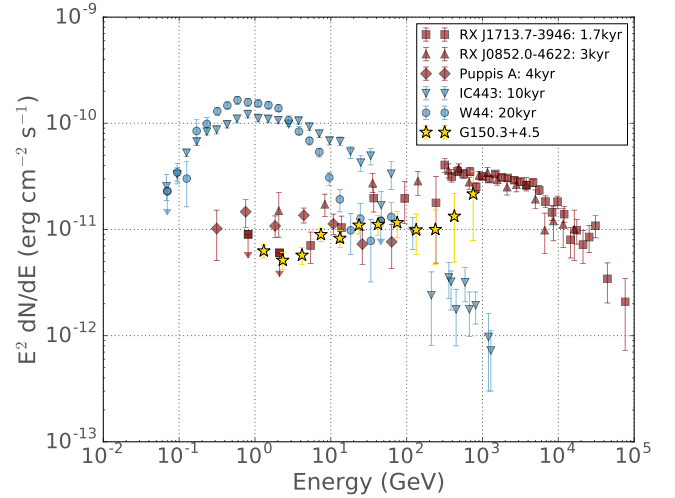
Having associated the  $\gamma$ -ray emission with SNR G150.3+4.5, next, we assessed the evolutionary state of the remnant to place it in context within the current population of LAT SNRs. Employing a standard Sedov-Taylor solution for the expansion of a blast wave, we estimated the age of G150.3+4.5. In the Sedov phase, the radius of the shock front is given by,

$$R_{ST} = 0.314 \left( \frac{E_{51}}{n_0} \right)^{1/5} t_{\text{yr}}^{2/5} \text{ pc}, \quad (1)$$

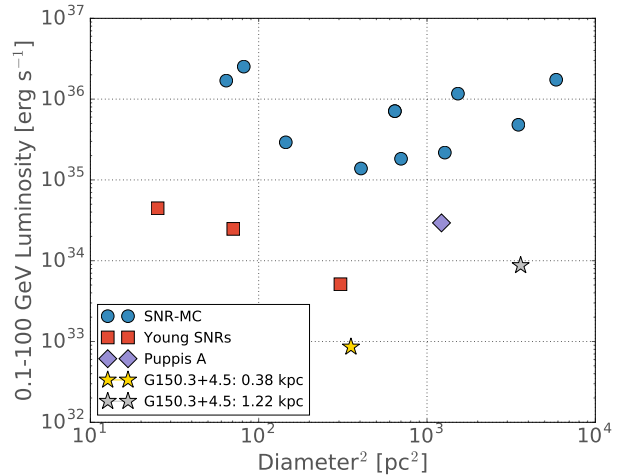
where  $E_{51}$  is the kinetic energy output of the supernova in units of  $10^{51}$  erg, and  $n_0$  the ambient density the shock is expanding into in units of  $\text{cm}^{-3}$ . Using the most viable HI kinematic distance,  $d \approx 0.38$  kpc (derived in §3.1), we showed that the projected radius of G150.3+4.5 is  $R \approx 9.4$  pc, and the corresponding ambient density (derived from the X-ray analysis in §3.2) is  $n_0 = 0.008 \text{ cm}^{-3}$ . Assuming a standard value of 1 for  $E_{51}$  we solved equation 1 for  $t_{\text{yr}}$  (the current age of the remnant in years) and used the derived values of  $R$  and  $n_0$  to estimate the age of the SNR as  $t \approx 0.44$  kyr. If instead we use a radius of 30 pc (see 3.1), with the corresponding ambient density  $n_0 = 0.005 \text{ cm}^{-3}$ , the age of G150.3+4.5 is  $t \approx 6.0$  kyr. Noting that our density estimate is atypically low with respect to other young SNRs, we also estimated the SNR age for a density of  $n_0 = 0.1 \text{ cm}^{-3}$ , which is more typical of dynamically young SNRs. We calculated an age of  $t \approx 1.5$  kyr for the radius determined from the near HI velocity and  $t \approx 28$  kyr for an SNR radius of 30 pc at this density.

Figure 6 shows the LAT SED of G150.3+4.5 overlaid on the spectra of a selection of other LAT observed SNRs with ages ranging from  $\sim 10^3 - 10^4$  yr. G150.3+4.5 exhibits a hard spectrum extending to TeV energies with no spectral break (breaks are commonly observed at a few GeV in LAT SNRs interacting with nearby molecular material (Hewitt & Lemoine-Goumard 2015)) and appears spectrally similar to the dynamically young SNRs like RX J1713.7-3946 and RX J0852.0-4622. In figure 7, we plotted the luminosity of several LAT SNRs against their squared diameters (a proxy for age, as evident from equation 1). With its low luminosity, G150.3+4.5 appears to correlate well with the younger set of LAT SNRs. Our age estimate alone does not unambiguously determine the evolutionary state of G150.3+4.5. However, when combined with the results of Figures 6 and 7 comparing G150.3+4.5 to the population of other LAT SNRs, it indicates that G150.3+4.5 is more compatible

with a dynamically unevolved, non-interacting (with the surrounding interstellar medium) stage of expansion.



**Figure 6.** SEDs for several LAT observed SNRs with ages spanning  $\sim 10^3 - 10^4$  yr. SNRs less than 10 kyr are plotted red, older blue. The GeV spectrum of G150.3+4.5 is shown as stars. SED references: RX J1713.7-3946; Abdo et al. (2011), RX J0852.0-4622; Tanaka et al. (2011), Puppis A; Hewitt et al. (2012), IC443 and W44; Ackermann et al. (2013)



**Figure 7.** 0.1-100 GeV luminosity of several LAT SNRs plotted against the SNR's diameter squared. Gold star corresponds to G150.3+4.5 lying at a distance of 0.38 kpc, silver to G150.3+4.5 being at 1.22 kpc. Blue circles are LAT detected SNRs known to be interacting with nearby molecular clouds. Red squares are young SNRs. The purple diamond represents Puppis A, which is a middle-aged SNR not known to be interacting with molecular material. This plot was reproduced (with the addition of G150.3+4.5) from Abramowski et al. (2015).

#### 4.3. Nonthermal Modeling

SNR shock fronts are known to be capable of accelerating cosmic rays to very high energies (Ackermann et al. 2013; Koyama et al. 1995). There are potentially multiple radiation mechanisms operating at the shock that produce GeV  $\gamma$ -rays. Accelerated electrons can give rise



to inverse Compton (IC) emission via upscattering of ambient cosmic microwave background (CMB), stellar, and IR photon fields, as well as non-thermal bremsstrahlung radiation. Energetic protons can collide with ambient protons in the surroundings, producing neutral pions which decay into  $\gamma$ -ray photons.

To infer the properties of the underlying relativistic particle populations in the SNR environment, it is vital to understand the origin of the observed  $\gamma$ -ray emission detected from G150.3+4.5. To do so, we employ the **naima** Python package. **naima** is an open-source code base that computes the non-thermal radiation from a relativistic particle population (Zabalza 2015). It utilizes known parameterizations and analytic approximations to the various non-thermal processes (i.e., synchrotron, IC, bremsstrahlung, and pion decay emission), which results in the calculations being computationally inexpensive. **naima** also makes use of **emcee**, a Markov chain Monte Carlo (MCMC) ensemble sampler for Bayesian parameter estimation (Foreman-Mackey et al. 2013). The sampler is used to find the best-fit parameters of the radiative models to the observed photon SED for a given particle distribution function.

To determine the best fit parameters, **naima** calls **emcee** to sample the log-likelihood function (i.e., the likelihood of the observed data given the assumed spectrum) of the radiative model. The radiative models require as input a particle distribution function to model the present-age electron or proton spectrum. We used a one-zone, homogeneous particle distribution model (which **naima** inherently assumes) and scaled the likelihood function by a uniform prior probability distribution. For this work, we model the separate proton and electron spectra as power laws with an exponential cut off,

$$\frac{dN}{dE_{(e,p)}} = A_{(e,p)} (E/E_0)^{-s} \exp\left(\frac{-E}{E_{\text{cutoff}}(e,p)}\right) \quad (2)$$

where  $E$  is the particle energy,  $E_0$  the reference energy,  $s$  the spectral index, and  $E_{\text{cutoff}}$  the cutoff energy. The electron distribution's normalization is related to the proton normalization through the electron-to-proton ratio scaling factor,  $A_e = K_{ep} A_p$ . We also assumed that the electron and proton distributions have the same spectral shape. For our radiation models, we fixed the ambient gas density and tested several values (as informed by the values determined in §3.2) for proton-proton and bremsstrahlung interactions. For IC emission, we include a CMB, FIR, and NIR component. [JAM: Talk about free/ fixed params of the model, reference the table, and figure to show best fit, discuss results and what the fits imply regarding lep/had dom and energy in e- p.]

[JAM: Used radio SED from (Gerbrandt et al. 2014)]  
[JAM: Say something about what the radio index is and the connection to the gev index]

[JAM: Discuss implications of the naima fits. Do they show preference for lep/had. Is total energy content in particles reasonable for different runs?]

[JAM: include the other few models I fit]

[JAM: looks like young SNRs, but no x-ray and lower luminosity than most other LAT SNRs. ROSAT is not

**Table 2**  
Naima Model Best Fit Parameters

s	$K_{ep}$	$A_p$	$B^a$	$E_{\text{cutoff}(e)}$	$E_{\text{cutoff}(p)}$
Fixed $K_{ep} = 0.01$					
$1.5 \pm 0.2$	0.01	-32.850	49.80	LMC	2
Fixed $K_{ep} = 0.1$					
$1.5 \pm 0.2$	0.1	-3.277	63.87	Puppis A	2
Fixed $K_{ep} = 1$					
$1.5 \pm 0.2$	1	-3.277	63.87	Puppis A	2
Fixed s					
$2 \pm 0.2$	1	-3.277	63.87	Puppis A	2

**Note.** — [JAM: add better caption] Results from **naima** model? Right now the free params are index,  $k_{ep}$ ,  $e_{\text{leccut}}$ ,  $prot_{\text{cut}}$ ,  $B$ . Fixed are  $n_h$ , all the IC photon field values distance (this is just for determining flux) [JAM: Correct values aren't in yet][JAM: add units to params]

<sup>a</sup> Calculated in **gtlike**

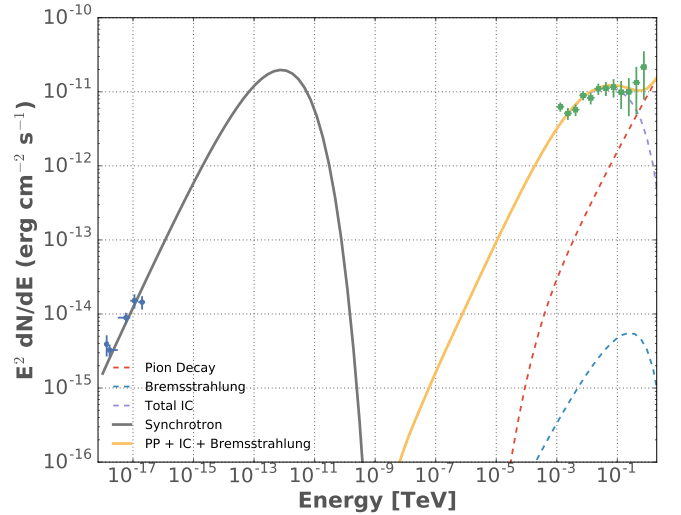


**Figure 8.** Non-thermal emission model for G150.3+4.5.

sensitive enough.]

[JAM: Deeper x-ray observations to search for the compact stellar remnant. ROSAT all-sky not that sensitive, dedicated X-ray to search for thermal/nonthermal components]

[JAM: Will HAWC be able to say anything? Is the extrapolated flux above the HAWC sensitivity?]

## 5. CONCLUSIONS

We analyzed 7 years of *Fermi*-LAT data in the direction of SNR G150.3+4.5, lowering the energy threshold from that previously reported in the 2FHL catalog, and report detection of significantly extended  $\gamma$ -ray emission coincident with the entirety of the radio remnant's shell. We find the emission from 1 GeV to 1 TeV to be well described by a power law of spectral index  $\Gamma = 1.82 \pm 0.04$ , with morphology consistent with a uniform disk with best-fit radius,  $\sigma = 1.40^\circ \pm 0.03^\circ$ . Based on radio and  $\gamma$ -ray properties of emission in the direction of G150.3+4.5, within the context of the current LAT SNR population, we argued that the GeV emission likely originates in the shock of G150.3+4.5, and disfa-

vor a PWN origin. To estimate the distance to the SNR, we obtained an HI spectrum toward G150.3+4.5 from the Leiden/Argentine/Bonn survey of Galactic HI. Calculating distances from the derived HI velocity peaks, we showed that the most reasonable distance estimate places G150.3+4.5 at a distance of  $d = 0.4$  kpc, potentially making it one of the closest known SNRs detected by the LAT [JAM: say something about implications and complications with this]. Using this distance and a standard Sedov-Taylor SNR evolution model, we estimate the age of the G150.3+4.5 to be  $t \sim 5$  kyr. To assess the underlying particle population acting in G150.3+4.5 we use the *naima* Python package to fit the observed radio and  $\gamma$ -ray SED to non-thermal electron and proton radiation models. [JAM: what the *naima* models suggest, and G150 fitting in with the younger LAT population. XMM x-ray observations to find PWN and CCO plus HAWX for TeV would help shed light on this]

## 6. SCRATCH

$L_\gamma = 1.3 \times 10^{33}$  erg s $^{-1}$  from 1 GeV to 1 TeV for best d and flux above  
 energy flux from 100 MeV to 100 GeV:  
 $4.84 \times 10^{-11}$  erg cm $^{-2}$  s $^{-1}$   
 $L_\gamma = 8.6 \times 10^{32}$  erg s $^{-1}$  from 100 MeV to 100 GeV for best d and flux in same range  
 energy flux from 1 GeV to 100 GeV:  
 $3.83 \times 10^{-11}$  erg cm $^{-2}$  s $^{-1}$   
 $L_\gamma = 6.8 \times 10^{32}$  erg s $^{-1}$  from 1 GeV to 100 GeV for best d and flux in same range  
 For diamMax = 60pc, dmax = 1.22kpc, and Lmax (100mev-100GeV) = 8.7e+33  
 [JAM: for synchrotron  $\alpha = (1-s)/2$ , where  $\alpha$  is the radio spectral index, and  $s$  the electron distribution power law index. Same for IC below break]  
 [JAM: For energies below the high energy break, For pion and brems  $\Gamma = 2\alpha + 1$  For IC,  $\Gamma = \alpha + 1$  ) for positive  $\alpha$ ]  
 [JAM: From Gaensler & Slane (2006) Typical indices for PWNe are  $\sim -0.3 \lesssim \alpha \lesssim 0$  in the radio band, and

( $\Gamma \approx 2$ ) in the X-ray band. So  $\alpha$  is not inconsistent, but at the boundary.]

## REFERENCES

- Abdo, A. A., et al. 2011, ApJ, 734, 28 6  
 —. 2013, ApJS, 208, 17 2.1  
 Abramowski, A., et al. 2015, A&A, 574, A27 7  
 Acero, F., et al. 2015, ApJS, 218, 23 2.1  
 —. 2016, ApJS, 224, 8 1  
 Ackermann, M., et al. 2012, ApJS, 203, 4 2.1  
 —. 2013, Science, 339, 807 1, 6, 4.3  
 —. 2016, ApJS, 222, 5 1, 2.1, 2.2  
 Atwood, W., et al. 2013a, ArXiv:1303.3514 1  
 Atwood, W. B., et al. 2009, ApJ, 697, 1071 2.1  
 —. 2013b, ApJ, 774, 76 1  
 Badenes, C., Maoz, D., & Draine, B. T. 2010, MNRAS, 407, 1301 3.1  
 Barr, E. D., et al. 2013, MNRAS, 429, 1633 2.2, 4.1  
 Chatterjee, S., et al. 2005, ApJL, 630, L61 4.1  
 Condon, J. J., Cotton, W. D., Greisen, E. W., Yin, Q. F., Perley, R. A., Taylor, G. B., & Broderick, J. J. 1998, AJ, 115, 1693 2.2  
 Foreman-Mackey, D., Hogg, D. W., Lang, D., & Goodman, J. 2013, PASP, 125, 306 4.3  
 Gaensler, B. M., & Slane, P. O. 2006, ARA&A, 44, 17 4.1, 6  
 Gao, X. Y., & Han, J. L. 2014, A&A, 567, A59 1, 2.2, 3.1, 4.1  
 Gerbrandt, S., Foster, T. J., Kothes, R., Geisbüsch, J., & Tung, A. 2014, A&A, 566, A76 1, 4.1, 4.3  
 Hewitt, J. W., Grondin, M.-H., Lemoine-Goumard, M., Reposeur, T., Ballet, J., & Tanaka, T. 2012, ApJ, 759, 89 6  
 Hewitt, J. W., & Lemoine-Goumard, M. 2015, Comptes Rendus Physique, 16, 674 4.2  
 Jogler, T., & Funk, S. 2016, ApJ, 816, 100 1  
 Kerr, M. 2010, PhD thesis, University of Washington, arXiv:1101.6072 2.1  
 Koyama, K., Petre, R., Gotthelf, E. V., Hwang, U., Matsuura, M., Ozaki, M., & Holt, S. S. 1995, Nature, 378, 255 4.3  
 Lande, J., et al. 2012, ApJ, 756, 5 2.1, 2.2  
 Reid, M. J., et al. 2014, ApJ, 783, 130 3.1  
 Reynolds, S. P. 2008, ARA&A, 46, 89 1  
 Tanaka, T., et al. 2011, ApJL, 740, L51 6  
 Voges, W., et al. 1999, A&A, 349, 389 3.2  
 Wootten, A. 1981, ApJ, 245, 105 3.1  
 Wootten, H. A. 1977, ApJ, 216, 440 3.1  
 Xu, Y., Reid, M. J., Zheng, X. W., & Menten, K. M. 2006, Science, 311, 54 3.1  
 Zabalza, V. 2015, ArXiv e-prints 4.3